Effects of piezoelectric energy harvesting from a morphing flapping tail on its performance

Hossam Alqaleiby^a, Mahmoud Ayyad^a, Muhammad R. Hajj^a, Saad A. Ragab^b, Lei Zuo^c

Abstract

Monitoring fish migration, which can extend over distances of thousands of kilometers, via fish tags is important to maintain healthy fish stocks and preserve biodiversity. One constraint of current fish tags is the limited power of their batteries. Attaching a piezoelectric element to an oscillating part of the fish body has been proposed to develop self-powered tags. To determine the functionality and potential of this technology, we present an analysis showing variations of the generated voltage with specific aspects of the tail's response. We also perform numerical simulations to validate the analysis and determine the effects of attaching a piezoelectric element on performance metrics including thrust generation, propulsive efficiency, and harvested electric power. The tail with the attached piezoelectric element is modeled as a unimorph beam moving at a constant forward speed and excited by sinusoidal pitching at its root. The hydrodynamic loads are calculated using three-dimensional unsteady vortex lattice method. These loads are coupled with the equation of motion, which is solved using the finite element method. The implicit finite different scheme is used to discretize the time-dependent generated voltage equation. The analysis shows that the harvested electric power depends on the slope of the trailing edge, a result that is validated with the numerical simulations. The numerical simulations show that, depending on the excitation frequency, attaching a piezoelectric element can increase or decrease the thrust force. The balance of required hydrodynamic power, generated propulsive power and harvested electrical power shows that, depending on the excitation frequency, relatively high levels of harvested power can be harvested without a high adverse impact on the hydrodynamic or propulsive power. For a specified frequency of oscillations, the approach and results can be used to identify design parameters where harvested electrical power by a piezoelectric element will have a minimal adverse impact on the hydrodynamic or propulsive power of a swimming fish.

Keywords: Fish tags, Piezoelectric energy harvesting, Finite-element method, Flexible fish tail, Three-dimensional unsteady vortex lattice method

 $Email\ address:\ {\tt haboalel@stevens.edu}\ ({\tt Hossam}\ {\tt Alqaleiby})$

^a Davidson Laboratory, Department of Civil, Environmental and Ocean Engineering, Stevens Institute of Technology, Hoboken, NJ 07030, USA.

^bBiomedical Engineering and Mechanics, Virginia Tech, Blacksburg, VA 24061, USA.

^cNaval Architecture and Marine Engineering, University of Michigan, Ann Arbor, MI 48103, USA.

1. Introduction

Continuous assessment of fish migration, movement patterns, and fishing levels is important to maintain healthy fish stocks [1, 2] and biodiversity [3]. Examples of wild fish groups for which migration and movement behavior have been studied include bluefin tuna [4], basking sharks [5], manta rayes [6], and saithe [7]. In these and other studies, the monitoring is performed using electronic tags that are either externally attached to the fish or surgically implanted in the fish. These tags transmit an acoustic signal to receivers using battery-powered transmitters. The weight, volume and finite energy of today's batteries limit their operational lifetime, which requires periodic replacement if possible and may affect the fish health [8]. Furthermore, in the case of relatively small fish, reducing the tag size necessitates a reduction in the battery size, which reduces its operational life [8]. For example, the lifetime of MB306 batteries used in the Juvenile Salmon Acoustic Telemetry System [9] is of the order of few days [10]. In contrast, fish migration, which involves relocation of fish groups from one area or body of water to another, can last for one year.

As an alternative to battery-powered tags with limited lifetime, self-powered fish tags provide the capability of monitoring fish populations over longer periods. Noting the energy associated with fish body's motions, one approach for powering these tags is to harvest energy from a piezoelectric (PZT) element that is attached or implanted in a moving part of the fish body such as its tail for energy harvesting purpose. This has been inspired from different demonstrations of vibration energy harvesting [11–21]. Li et al. [22] developed a self-powered acoustic transmitter that harvests energy from the deformation of the fish body while swimming. The unit consists of a flexible piezoelectric composite beam, a circuit board and a transducer. It is about 10 cm long, has a volume of 0.57 cm^3 , and weighs about 1 gram. It emits a 150 dB signal having unique tag codes that can be detected up to 100 meters away [22]. The amount of energy generated depends on the degree of the body bending during swimming. Other experimental studies that demonstrated the use of PZT to harvest energy from a fish-like motion include harvesting energy from bimorph cantilevers [23], a flying pigeon [24], and a biomimetic fish tail [25]. Cha et al. [26] harvested energy from fish swimming using ionic polymer-metal composites, while Zhang et al. [27] used multilayer-structured triboelectric nanogenerator to harvest undersea energy on a bionic-fin. Qian et al. [28] designed a bio-inspired bi-stable beam that can efficiently harvest energy if attached to a fish body. Numerical studies have also been performed to investigate energy harvesting from fish-like motions. Salazar et al. [29] numerically investigated the energy harvesting from a PZT element attached to a carangiform fish body. They prescribed the fish motion as a travelling wave along the fish body length [30]. Sun et al. [31] studied energy harvesting from an inward-type flow device undulating in a fish-like motion. Chen et al. [32] modeled a tail as a rigid element with a flexible PZT generator attached to its end to harvest energy.

Although many studies demonstrated the capability of harvesting energy from fish-like motions, few of them addressed the impact of attaching PZT energy harvesters on the propulsive performance of the fish. Attaching the PZT element changes the local stiffness and the harvested power could reduce the thrust and effectiveness of the swimming action of the fish. Furthermore, there is not a validated analytical treatment that associates the generated power with

a physical quantity of the undulating motion that can be used in the initial assessment and design of a PZT element based on fish size. Here, we perform analysis and numerical simulations of the effects of attaching a PZT to a flexible element such as a fish tail or caudal fin on its hydrodynamic performance in terms of generating thrust. The PZT element is made of a thin macro fiber composite (MFC), which is increasingly applied in engineering, due to its high flexibility and strong actuation forces [33]. Furthermore, it was demonstrated to minimize the burden on the fish body as noted by Li et al. [22]. For modeling purposes, the tail is represented by a beam having an aspect ratio equal to one and the PZT element is assumed to cover the whole tail. As such, the tail is modeled as a thin unimorph cantilever beam that is excited by sinusoidal pitching at its root. Although an operational fish tag would include a more complex circuit that requires a rechargeable battery or a capacitor [22], we limit the study here, which is concerned with impact of harvesting energy on the fish performance, to a resistive electrical load. The three-dimensional Unsteady Vortex Lattice Method (UVLM) [34] is used to calculate the hydrodynamic loads generated by the pitching excitation under constant forward speed. These include the thrust and transverse force and the required power. The finite element method is used to solve the coupled time-dependent equations of motion representing the fluid-structure interaction. The implicit finite different scheme is used to discretize the time-dependent generated voltage equation. The coupled equations of motions are solved for structural deformation of the tail, based on the hydrodynamic load, at each time step where the generated voltage is updated.

2. Methods

We model the fish tail as a flexible thin rectangular substrate with chord length c, span b, and thickness h_s . To harvest energy, we attach a PZT MFC layer to the top of the substrate as shown in figure 1a. This layer has a thickness h_p and covers the entire length and width of the substrate beam. In the following, we refer to this composite beam, including the substrate and PZT layers, as unimorph PZT tail or simply tail. The PZT layer is connected to a resistive electrical load. We assume that the tail moves with a uniform forward speed U_{∞} and is excited by sinusoidal pitching, $\theta(t) = \theta_o \sin(\omega t)$, at its root, as shown in figure 1b. We neglect the flexibility in the spanwise direction for the range of flexibility considered herein based on the experimental observations by Dewey et al. [35].

2.1. Governing equations

2.1.1. Tail deflection

The Euler-Bernoulli beam theory is used to model the deflection of the flexible unimorph tail due to pitching excitation at the root and hydrodynamic loads. To derive the governing equation, we consider a general point p on the composite beam where, as schematically shown in figure 1b, two frames of reference are used to describe the dynamics of point p. The first one is the inertial frame of reference attached to the fish body and defined by X-, Y-, and Z-axes representing the forward, rotational, and lateral motions, respectively. The second one is the rotating local frame of reference attached to the beam's leading edge and defined by x-, y-, and z-axes such that the rotating y-axis is coincident

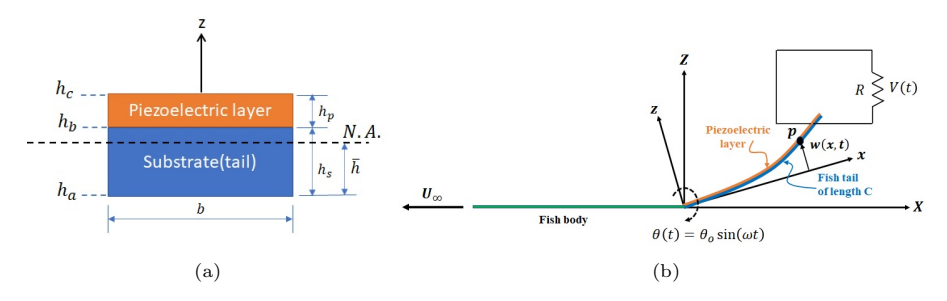


Figure 1: (a) Cross section and position of neutral axis (N.A.) for the unimorph piezoelectric tail. (b) Schematic representation and coordinate systems used in modeling the tail's oscialtions.

with the inertial rotating Y-axis as shown in the figure. The position $\vec{\mathbf{r}}_p$, and angular velocity $\vec{\Omega}$ vectors of point p in the rotating frame of reference are given by

$$\vec{\mathbf{r}}_p = x\hat{\mathbf{i}} + w\hat{\mathbf{k}} \tag{1}$$

and

$$\vec{\Omega} = \dot{\theta}\hat{\mathbf{j}} \tag{2}$$

where $\hat{\mathbf{i}}$, $\hat{\mathbf{j}}$, and $\hat{\mathbf{k}}$ are respectively the unit vectors in the x-, y-, and z-directions, x is the radial distance from the root and w is the transverse deflection in the x-z plane, and $\hat{\theta}$ is the angular speed of the pitching excitation at the root in the y-axis. The velocity, $\vec{\mathbf{V}}_p$, and acceleration, $\vec{\mathbf{a}}_p$, of point p in the inertial frame of reference are respectively given by

$$\vec{\mathbf{V}}_{p} = \frac{d\vec{\mathbf{r}}_{p}}{dt} \bigg|_{I} = \frac{d\vec{\mathbf{r}}_{p}}{dt} \bigg|_{R} + \vec{\mathbf{\Omega}} \times \vec{\mathbf{r}}_{p} = \dot{\theta} w \hat{\mathbf{i}} + (\dot{w} - \dot{\theta} x) \hat{\mathbf{k}}$$
(3)

and

$$\vec{\mathbf{a}}_{p} = \frac{d\vec{\mathbf{V}}_{p}}{dt} \bigg|_{I} = \frac{d\vec{\mathbf{V}}_{p}}{dt} \bigg|_{R} + \vec{\mathbf{\Omega}} \times \vec{\mathbf{V}}_{p} = \left(\ddot{\theta}w + 2\dot{\theta}\dot{w} - \dot{\theta}^{2}x \right) \hat{\mathbf{i}} + \left(\ddot{w} - \ddot{\theta}x - \dot{\theta}^{2}w \right) \hat{\mathbf{k}} = a_{x}\hat{\mathbf{i}} + a_{z}\hat{\mathbf{k}}$$

$$\tag{4}$$

where the subscripts I and R represent respectively the inertial and rotating frames of reference, () represents the time derivative of the variable, and a_x and a_z are the x-, and z-components of the inertial acceleration.

We follow the approach of Hussein et al. [36] to derive the governing equations for the response of the unimorph tail. We also assume that the extension of the mid-plane is zero, i.e. the beam is in-extensible. The dynamic equilibrium equation in the x-direction, based on the free-body and kinetics diagrams of a beam element of mass m per unit length and length dx, as shown in Figure 2 is written as

$$dT \approx ma_x dx = m \left(\ddot{\theta} w + 2\dot{\theta} \dot{w} - \dot{\theta}^2 x \right) dx \tag{5}$$

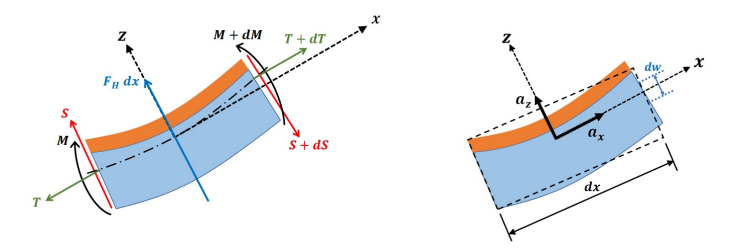


Figure 2: Free-body (left sketch) and kinetics (right sketch) diagrams of a general composite beam element centered at point p.

where dT is the differential tension force. To obtain the tension force distribution T(x) along the tail length, we integrate equation (5) from any arbitrary point x along the tail to the trailing edge. The resultant tension force distribution is given as

$$T(x) = \frac{m\dot{\theta}^2}{2} \left(c^2 - x^2 \right) - m \int_x^c \left(\ddot{\theta}w + 2\dot{\theta}\dot{w} \right) dx \approx \frac{m\dot{\theta}^2}{2} \left(c^2 - x^2 \right) \tag{6}$$

where the integral term is neglected because w is much smaller than θx . The mass per unit length, m, of the unimorph piezoelectric tail is given by

$$m = \rho_s h_s b + \rho_p h_p b \tag{7}$$

where ρ_s and ρ_p are the densities of the substrate and PZT materials, respectively.

The equation of dynamic equilibrium in the z-direction is written as

$$F_H dx - dS = ma_z dx = m\left(\ddot{w} - \ddot{\theta}x - \dot{\theta}^2 w\right) dx \tag{8}$$

where $F_H dx$ is the normal hydrodynamic force acting on the element as a result of the pitching excitation $\theta(t)$ and the uniform forward speed U_{∞} , and dS is the differential shear force. The equilibrium equation of the sum of moments yields

$$dM - Tdw - Sdx = 0 (9)$$

where the moment due to the normal hydrodynamic forces is neglected when compared to the other terms. By substituting equation (9) in (8), the governing equation of the beam deflection is written as:

$$\frac{\partial^2 M}{\partial x^2} - \frac{\partial}{\partial x} \left(T(x) \frac{\partial w}{\partial x} \right) + m \left(\ddot{w} - \ddot{\theta}x - \dot{\theta}^2 w \right) = F_H(w, \dot{w}, \ddot{w}) \tag{10}$$

The internal moment M can be calculated at any cross section by integrating the first moment of stress distribution over the corresponding area [37] as follows

$$M(x,t) = -\int_{h_a}^{h_b} T_1^s z b dz - \int_{h_b}^{h_c} T_1^p z b dz$$
 (11)

where T_1 is the axial stress. Here and hereafter, the subscripts and superscripts s and p are used to denote the substrate and PZT layers respectively, h_a and

 h_b are respectively the positions of bottom and top surfaces of the substrate from the neutral axis, while h_c is the top surface position of the PZT layer from this axis as defined in figure 1a. Denoting the distance from the bottom of the substrate to the neutral axis by \bar{h} , it is given by

$$\bar{h} = \frac{h_s}{2} + \frac{(h_p + h_s)E_p h_p}{2(E_p h_p + E_s h_s)}$$
(12)

where E_s and E_p are the Young's moduli of substrate and PZT layers, respectively. The positions h_a , h_b and h_c are then given by:

$$h_a = -\bar{h}, \qquad h_b = h_s - \bar{h}, \text{ and } \qquad h_c = (h_s + h_p) - \bar{h}$$
 (13)

The stress-strain relations are given by the constitutive equations of the substrate and PZT materials [38] as

$$T_1^s = E_s S_1^s T_1^p = E_p (S_1^p - d_{31} E_3)$$
(14)

where d_{31} is the PZT constant, and the 1- and 3-directions are coincident with x- and z-directions in the rotating frame of reference and E_3 is the electric field in the direction of polarization and is related to the electric potential difference across the PZT layer V(t) by

$$E_3(t) = \frac{-V(t)}{h_p} \tag{15}$$

The axial strain S_1 at any location x along the beam length and certain level z from the neutral axis is proportional with the curvature of the beam at the same location x and given by

$$S_1(x,z,t) = -z \frac{\partial^2 w(x,t)}{\partial x^2} \tag{16}$$

Substituting equations (14, 15, and 16) into equation (11), the internal moment is rewritten in terms of the curvature of the beam and the generated voltage as follows:

$$M(x,t) = EI\frac{\partial^2 w(x,t)}{\partial x^2} + \Theta V(t) \left[H(x) - H(x-c) \right]$$
(17)

where EI is the flexural rigidity of the unimorph tail that is given by

$$EI = E_s b \left(\frac{h_b^3 - h_a^3}{3} \right) + E_p b \left(\frac{h_c^3 - h_b^3}{3} \right)$$
 (18)

and Θ is the electro-mechanical coupling term that is given by

$$\Theta = \frac{-E_p b d_{31} \left(h_c^2 - h_b^2\right)}{2h_p} = \frac{-e_{31} b (h_b + h_c)}{2} \tag{19}$$

where $e_{31} = E_p d_{31}$ is the PZT constant. We note that the second term of the internal moment expression in equation (17) is multiplied by [H(x) - H(x-c)],

where H(x) is the Heaviside function, to enable its differentiation, which is required when solving the governing equation (10). We also note that, if the PZT layer and/or the electrodes cover a region from x_1 to x_2 , then the second term of equation (17) will be multiplied by $[H(x-x_1) - H(x-x_2)]$.

Substitution of equation (17) into equation (10) yields the governing equation for the relation between the beam deflection and generated voltage term as

$$\frac{\partial^{2}}{\partial x^{2}} \left(EI \frac{\partial^{2} w}{\partial x^{2}} \right) - \frac{\partial}{\partial x} \left(T(x) \frac{\partial w}{\partial x} \right) + m \left(\ddot{w} - \ddot{\theta}x - \dot{\theta}^{2} w \right) + \Theta V(t) \left(\frac{d\delta(x)}{dx} - \frac{d\delta(x - c)}{dx} \right) = F_{H}(w, \dot{w}, \ddot{w})$$

$$(20)$$

where $\delta(x)$ is the Dirac delta function, obtained when taking the first derivative of the Heaviside function [39].

2.1.2. Generated electric power

To derive the governing equation for the generated electric power, we follow the procedure by Erturk and Inman [40]. First, Ohm's law is used to relate the generated voltage to the charge distribution resulting from the PZT strain change while Gauss law is used to determine the collected charges through the PZT layer [38]. Therefore, Ohm's law is written as

$$\frac{d}{dt} \int_{A} \mathbf{D.n} \ dA = \frac{V(t)}{R} \tag{21}$$

where the integration is performed over the electrode area A [37, 38], \mathbf{D} is the vector of the electric displacement components in the PZT layer, \mathbf{n} is the the outward normal unit vector, V is the generated voltage, and R is the electrical load resistance. The inner product of the integrand gives only the displacement components in the direction normal to the surface of the PZT layer, i.e., the z- or 3-direction, and since the only source of mechanical strain is assumed to be the axial strain due to bending, the constitutive equation of the PZT displacement vector [38] is written as

$$D_3 = e_{31} S_1^p + \varepsilon_{33}^s E_3 \tag{22}$$

where ε_{33}^S is the permittivity component at constant strain, and S_1^p is the axial strain component of the PZT layer at its centroid which is calculated from equation (16). Inserting equation (15) into equation (22), and using the Gauss law in equation (21), knowing that dA = bdx, the governing equation for the harvested voltage is expressed as

$$\frac{V(t)}{R} + \tilde{C}_p \frac{dV(t)}{dt} - \Theta \int_0^c \frac{\partial^3 w(x,t)}{\partial x^2 \partial t} dx = 0$$
 (23)

where \tilde{C}_p is the PZT layer capacitance defined as

$$\tilde{C}_p = \frac{\varepsilon_{33}^s bc}{h_p} \tag{24}$$

Applying the zero slope boundary condition at the root, i.e. at x=0 in equation (23), yields

$$\frac{V(t)}{R} + \tilde{C}_p \dot{V}(t) - \Theta \dot{q}_c(t) = 0 \tag{25}$$

where \dot{q}_c represents the time rate of change of the slope of the trailing edge and is given by

$$\dot{q}_c(t) = \frac{\partial}{\partial t} \left(\frac{\partial w(x,t)}{\partial x} \right) \bigg|_{x=c}$$
 (26)

Noting the harmonic response of the flapping element and harvested power, and following the procedure of Tan et al. [41], we represent the slope of the trailing edge slope and voltage by harmonic functions and write

$$q_c(t) = \left(\frac{\partial w}{\partial x}\right)\Big|_{x=c} = \frac{1}{2}a_1e^{i\omega t} + cc$$

$$V(t) = \frac{1}{2}a_2e^{i\omega t} + cc$$
(27)

where i is the unit imaginary number and cc stands for the complex conjugate. The relation between a_1 and a_2 is governed by equation (25) and is given by

$$a_2 = \frac{\Theta \omega R}{\tilde{C}_p \omega R - i} a_1 \tag{28}$$

The root mean square voltage can then be directly expressed in terms of the trailing edge slope amplitude and written as

$$V_{rms} = \frac{R\Theta\omega}{\sqrt{\tilde{C}_p^2 \omega^2 R^2 + 1}} \frac{\left| \left(\frac{\partial w}{\partial x} \right)_{x=c} \right|}{\sqrt{2}}$$
 (29)

It is interesting to note here the proportional relation of the harvested voltage to the slope of the flapping beam at the trailing edge. The harvested electric power, $P = V_{rms}^2/R$, is used to determine an analytical expression for the optimum electrical load resistance R_{opt} and the corresponding maximum harvested electric power P_{max} as

$$R_{opt} = \frac{1}{\tilde{C}_{n}\omega}, \qquad P_{max} = \frac{\Theta^{2}\omega}{4\tilde{C}_{n}} \left| \left(\frac{\partial w}{\partial x} \right)_{max} \right|^{2}$$
 (30)

Equation (30) provides an analytical expression for the direct dependence of the maximum generated power on the frequency of the excitation and on the amplitude of the response, which, in turn, is dependent on the amplitude and frequency of the excitation as applied at the root of the unimorph tail.

2.2. Hydrodynamic forces and power calculations

To determine the hydrodynamic forces, we implement the three-dimensional unsteady vortex lattice method (UVLM) approach [42–44] that captures added mass forces, variations in the bound circulation, wake, and induced drag associated with the swimming action. Details about implementing the three-dimensional UVLM and the solution of the coupled fluid-structure interaction can be found in [36, 45, 46]. In summary, the flow is assumed to remain attached over the tail, which is represented by a bound vortex sheet discretized as vortex rings over $N_x \times N_y$ panels, where N_x and N_y are respectively the

number of panels in the x- and y-directions. Hussein et al. [36] determined that $N_x = 8$, $N_y = 10$ and non-dimensional time step of $(c\Delta t/U_{\infty} = 1/(4N_x + 1))$ are sufficient to yield grid independent solution. The total force vector from all panels is given by

$$\vec{\mathbf{F}} = \sum_{i}^{N_x} \sum_{j}^{N_y} \vec{\mathbf{F}}_{i,j} = (F_X, F_Y, F_Z)$$
(31)

The input aerodynamic power at the leading edge is calculated from the hydrodynamic power required to flap the tail and is calculated as

$$P_{in} = \sum_{i}^{N_x} \sum_{j}^{N_y} \left(\vec{\mathbf{r}}_{oi,j} \times \vec{\mathbf{F}}_{i,j} \right) \cdot \vec{\mathbf{\Omega}}$$
(32)

where $\vec{\mathbf{r}}_{oi,j}$ is the position vector from the leading edge to the center of each panel. The propulsive (output) power is defined as

$$P_{out} = \left(\vec{\mathbf{F}} \cdot \hat{\mathbf{I}}\right) U_{\infty} = F_X U_{\infty} \tag{33}$$

The propulsive efficiency η_p , transverse force coefficient C_L , thrust coefficient C_T , and power coefficient C_P are calculated as

$$\eta_p = \frac{\overline{P}_{out}}{\overline{P}_{in}}, \qquad C_L = \frac{\overline{F}_Z}{\frac{1}{2}\rho U_\infty^2 bc}, \qquad C_T = \frac{\overline{F}_X}{\frac{1}{2}\rho U_\infty^2 bc}, \text{ and } \qquad C_P = \frac{\overline{P}_{in}}{\frac{1}{2}\rho U_\infty^3 bc}$$
(34)

where $\overline{()}$ refers to the mean value.

2.3. Solution of the coupled model

2.3.1. Numerical discretization

Using a second order implicit finite difference representation, equation (25) is written as a difference equation that relates the voltage at time m+1 to the voltage at time m by

$$\frac{1}{R} \left(\frac{V^{m+1} + V^m}{2} \right) + \tilde{C}_p \left(\frac{V^{m+1} - V^m}{\Delta t} \right) - \Theta \left(\frac{\dot{q_c}^{m+1} + \dot{q_c}^m}{2} \right) = 0 \quad (35)$$

or

$$V^{m+1} = -\frac{\eta_2}{\eta_1} V^m + \frac{\Theta}{2\eta_1} \left(\dot{q_c}^{m+1} + \dot{q_c}^m \right)$$
 (36)

where

$$\eta_1 = \frac{1}{2R} + \frac{\tilde{C}_p}{\Delta t}, \text{ and } \eta_2 = \frac{1}{2R} - \frac{\tilde{C}_p}{\Delta t}$$
(37)

The finite element method is also used to discretize the space operator in the equation of motion (20) by multiplying the residual by a weight function (\tilde{w}^T)

and integrating over the generic finite element length. Rearranging the terms, equation (20) is rewritten as

$$[\mathbf{M}]\{\ddot{\mathbf{q}}\} + [\mathbf{K}]\{\mathbf{q}\} + \Theta V(t) \left(\{\mathbf{R}_o\} + \{\mathbf{R}_c\}\right) = \{\mathbf{F}(\mathbf{q}, \dot{\mathbf{q}}, \ddot{\mathbf{q}})\}$$
(38)

where [M] is the mass matrix, [K] is the stiffness matrix, and $\{\mathbf{F}(\mathbf{q}, \dot{\mathbf{q}}, \ddot{\mathbf{q}})\}$ is the time-dependent forcing vector containing the lateral force, forcing torque at the leading edge, and local hydrodynamic forces on the $N_x \times N_y$ nodal degrees of freedom \mathbf{q} . The integration of the voltage term yields two concentrated moment vectors defined at the leading $\{\mathbf{R}_o\}$ and trailing $\{\mathbf{R}_c\}$ edges, i.e. at the first and last finite element nodes. We use the Hermite polynomials to represent the distribution of \mathbf{q} over one element with two degrees of freedom at each node, including the transverse deflection (w) and slope $(\partial w/\partial x)$, i.e. $\mathbf{q} = \{w, \partial w/\partial x\}^T$. The above element matrices and vectors are calculated as follows

$$[\mathbf{M}] = m \int_0^l (N_w)^T N_w dx$$

$$[\mathbf{K}] = \int_0^l \left(EI(N_w'')^T N_w'' + \frac{m\dot{\theta}^2}{2} (N_w')^T \left(c^2 - (X_i + x)^2 \right) N_w' - m\dot{\theta}^2 N_w^T N_w \right) dx$$

$$\{\mathbf{R}_o\} = \int_0^l \frac{d\delta(x)}{dx} \tilde{w}^T dx = -\int_0^l \delta(x) \frac{dN_w^T}{dx} dx = -\frac{dN_w^T}{dx} \Big|_{x=0} = \{0, -1, 0, 0\}^T, \text{ for first element only }$$

$$\{\mathbf{R}_c\} = -\int_0^l \frac{d\delta(x-c)}{dx} \tilde{w}^T dx = \int_0^l \delta(x-c) \frac{dN_w^T}{dx} dx = \frac{dN_w^T}{dx} \bigg|_{x=l} = \{0,0,0,1\}^T, \text{ for last element only }$$

$$\{\mathbf{F}(\mathbf{q}, \dot{\mathbf{q}}, \ddot{\mathbf{q}})\} = \int_0^l \left(N_w^T F_H(q, \dot{q}, \ddot{q}) + m N_w^T \ddot{\theta} x \right) dx$$
(39)

where l is the element length, X_i is the starting coordinate of each element, $()' = \frac{\partial}{\partial x}$ is the derivative with respect to x, and N_w is the Hermite polynomials shape functions defined as

$$N_w = \frac{1}{l^3} \left\{ (l^3 - 3lx^2 + 2x^3), (xl^3 - 2l^2x^2 + lx^3), (3lx^2 - 2x^3), (-l^2x^2 + lx^3) \right\}$$
(40)

2.3.2. Time-marching scheme

We use the Newmark method [47, 48] for direct time integration of the equation of motion (38). Using equation (36), the discretized equation of motion over a local generic element is given as

$$[\mathbf{M}] \{\ddot{\mathbf{q}}\}^{m+1} + [\mathbf{C}] \{\dot{\mathbf{q}}\}^{m+1} + [\mathbf{K}] \{\mathbf{q}\}^{m+1} = \{\mathbf{F}(\mathbf{q}^{m+1}, \dot{\mathbf{q}}^{m+1}, \ddot{\mathbf{q}}^{m+1})\} + \Theta \frac{\eta_2}{\eta_1} \left(\{\mathbf{R}_o\} + \{\mathbf{R}_c\} \right) V^m - \frac{\Theta^2}{2\eta_1} \dot{q_c}^m \{\mathbf{R}_c\} + \frac{1}{2\eta_1} \dot{q_c}^m \{\mathbf{R}_c + \mathbf{R}_c\} + \frac{1}{2\eta_1} \dot{q_c}^m \{\mathbf{R}_c + \mathbf{R}_$$

(41)

The aforementioned substitution introduced matrix $[\mathbf{C}]$, which represents the slope of last node, i.e. trailing edge. After assembly, all entries in the global matrix $[\mathbf{C}]$ are zeros except for the last diagonal element which is $(\Theta^2/(2\eta_1))$. Similarly, all the entries in the global vector $\{\mathbf{R}_o\}$ are zeros except for the second array element which is -1 and the entries of the global vector $\{\mathbf{R}_c\}$ are all zeros except for the last array element which is 1.

The displacement $(\{\mathbf{q}\}^{m+1})$ and velocity $(\{\dot{\mathbf{q}}\}^{m+1})$ terms are updated based on Newmark method as

$$\{\mathbf{q}\}^{m+1} = \{\mathbf{q}\}^m + \{\dot{\mathbf{q}}\}^m \Delta t + \frac{1}{2}(1-\gamma)(\Delta t)^2 \{\ddot{\mathbf{q}}\}^m + \frac{1}{2}\gamma(\Delta t)^2 \{\ddot{\mathbf{q}}\}^{m+1}$$
 (42)

and

$$\{\dot{\mathbf{q}}\}^{m+1} = \{\dot{\mathbf{q}}\}^m + (1-\alpha)\Delta t \{\ddot{\mathbf{q}}\}^m + \alpha \Delta t \{\ddot{\mathbf{q}}\}^{m+1}$$

$$\tag{43}$$

where α and γ are set equal to 0.5 to ensure stability and accuracy of the Newmark method.

The acceleration and displacement equations at time (m+1) are respectively determined by substituting the velocity update equation (43) in the discretized equation of motion (41), and by substituting the acceleration equation in the displacement update equation (42). Performing these operations, we write the displacement and acceleration equations, respectively, in the form

$$[\mathbf{A}_{1}]\{\mathbf{q}\}^{m+1} = \{\mathbf{R}_{1}(\mathbf{q}^{m+1}, \dot{\mathbf{q}}^{m+1}, \ddot{\mathbf{q}}^{m+1})\}$$

$$[\mathbf{A}_{2}]\{\ddot{\mathbf{q}}\}^{m+1} = \{\mathbf{R}_{2}(\mathbf{q}^{m+1}, \dot{\mathbf{q}}^{m+1}, \ddot{\mathbf{q}}^{m+1})\}$$
(44)

where

$$[\mathbf{A}_1] = [\mathbf{M}] + \alpha \Delta t [\mathbf{C}] + \frac{1}{2} \gamma (\Delta t)^2 [\mathbf{K}]$$
$$[\mathbf{A}_2] = [\mathbf{M}] + \alpha \Delta t [\mathbf{C}]$$
(45)

and

$$\begin{aligned} \{\mathbf{R}_1\} = & [\mathbf{A}_2] \left(\{\mathbf{q}\}^m + \Delta t \{\dot{\mathbf{q}}\}^m + \frac{1}{2} (1 - \gamma) (\Delta t)^2 \{\ddot{\mathbf{q}}\}^m \right) + \frac{1}{2} \gamma (\Delta t)^2 \left(\{\mathbf{F}(\mathbf{q}^{m+1}, \dot{\mathbf{q}}^{m+1}, \ddot{\mathbf{q}}^{m+1}) \} \right) \\ & + \Theta \frac{\eta_2}{\eta_1} \left(\{\mathbf{R}_o\} + \{\mathbf{R}_c\} \right) V^m - \frac{\Theta^2}{2\eta_1} \dot{q}_c^m \{\mathbf{R}_c\} - [\mathbf{C}] \left(\{\dot{\mathbf{q}}\}^m + (1 - \alpha) \Delta t \{\ddot{\mathbf{q}}\}^m \right) \end{aligned}$$

$$\{\mathbf{R}_{2}\} = \left\{\mathbf{F}(\mathbf{q}^{m+1}, \dot{\mathbf{q}}^{m+1}, \ddot{\mathbf{q}}^{m+1})\right\} + \Theta \frac{\eta_{2}}{\eta_{1}} \left(\{\mathbf{R}_{o}\} + \{\mathbf{R}_{c}\}\right) V^{m} - \frac{\Theta^{2}}{2\eta_{1}} \dot{q}_{c}^{m} \{\mathbf{R}_{c}\} - \left[\mathbf{C}\right] \left(\{\dot{\mathbf{q}}\}^{m} + (1 - \alpha)\Delta t \{\ddot{\mathbf{q}}\}^{m}\right) - \left[\mathbf{K}\right] \{\ddot{\mathbf{q}}\}^{m+1}$$

$$(46)$$

Using the velocity update equation (43), the system of equations (44) is rewritten in terms of \mathbf{q} and $\dot{\mathbf{q}}$ as follows

$$[\mathbf{A}_{1}]\{\mathbf{q}\}^{m+1} = \{\mathbf{R}_{1}(\mathbf{q}^{m+1}, \dot{\mathbf{q}}^{m+1}, \ddot{\mathbf{q}}^{m+1})\}$$

$$[\mathbf{A}_{2}]\{\dot{\mathbf{q}}\}^{m+1} = \{\mathbf{R}_{3}(\mathbf{q}^{m+1}, \dot{\mathbf{q}}^{m+1}, \ddot{\mathbf{q}}^{m+1})\}$$

$$(47)$$

where

$$\left\{\mathbf{R}_{3}(\mathbf{q}^{m+1},\dot{\mathbf{q}}^{m+1},\ddot{\mathbf{q}}^{m+1})\right\} = \alpha \Delta t \left\{\mathbf{R}_{2}(\mathbf{q}^{m+1},\dot{\mathbf{q}}^{m+1},\ddot{\mathbf{q}}^{m+1})\right\} + \left[\mathbf{A}_{2}\right] \left(\left\{\dot{\mathbf{q}}\right\}^{m} + (1-\alpha)\Delta t \left\{\ddot{\mathbf{q}}\right\}^{m}\right)$$

$$(48)$$

To ensure stability of the solution, we solve equation (47) using the strong coupling (implicit) approach. Thus, equation (47) is rewritten as a system of algebraic equations in the form of

$$\mathbf{F}(\zeta) = \begin{bmatrix} \mathbf{A}_1 & 0 \\ 0 & \mathbf{A}_2 \end{bmatrix} \begin{Bmatrix} \{\mathbf{q}\}^{m+1} \\ \{\dot{\mathbf{q}}\}^{m+1} \end{Bmatrix} - \begin{Bmatrix} \{\mathbf{R}_1\} \\ \{\mathbf{R}_3\} \end{Bmatrix} = \{\mathbf{0}\}$$
(49)

where $\{\zeta\} = \{\{\mathbf{q}^{m+1}\}, \{\dot{\mathbf{q}}^{m+1}\}\}^T$. We use Newton-Raphson method to solve the system of equations (49) where the local iteration (k+1) is updated by

$$\boldsymbol{\zeta}_{k+1}^{m} = \boldsymbol{\zeta}_{k}^{m} - \left(\frac{\partial \mathbf{F}_{i}}{\partial \boldsymbol{\zeta}_{i}} | \boldsymbol{\zeta}_{k}^{m}\right)^{-1} \mathbf{F}(\boldsymbol{\zeta}_{k}^{m})$$
(50)

The convergence criterion is imposed on the displacement vector \mathbf{q} and defined by

$$\frac{||\mathbf{q}_{k+1}^m - \mathbf{q}_k^m||}{||\mathbf{q}_{k+1}^m||} \le \epsilon \tag{51}$$

When convergence is achieved, the tail form, i.e. deflection and slope, at the next time step is set to be the one from the last iteration of the current time step, i.e. $\mathbf{q}(t_0)^{m+1} = \mathbf{q}(t_{k+1}^m)$.

3. Results and Discussion

The geometric and material properties of the substrate and piezoelectric components of the unimorph tail are presented in table 1. The flexural rigidity of the substrate is set to $12.8 \times 10^{-3} Nm^2$, which is close to the near-root flexural rigidity values of the biological pectoral fin rays of the bluegill sunfish [49]. Additionally, the beam's aspect ratio is set equal to 1 and its mass ratio, defined as the relative magnitude of the fluid inertia with respect to the beam inertia is set equal to 45.4. All results are presented using the non-dimensional time $U_{\infty}t/c$ and non-dimensional excitation frequency, referred to as the reduced frequency, $k = \omega c/2U_{\infty}$ where ω is the angular frequency of the excitation. The considered range of the excitation frequency is between 2 and 13 Hz, which corresponds to a reduced frequency range between 1.7 and 11.27. All simulations were carried out for an excitation amplitude $\theta_o = 8^{\circ}$. We note that the selected range of frequencies between 2 and 13 Hz, the relative forward speed of 3.67 BL/s when represented in terms of the beam length (BL), and the range of resulting non-dimensional tail-flapping amplitude of about 0.2 correspond to observed parameters of swimming fish [50]. The composite bending stiffness EI $= 0.044 \ N.m^2$ is close to the bending stiffness of swimming fish and within the range required to generate propulsion [51].

Table 1: Tail and PZT parameters.

Parameter	Value
$\overline{c\ (mm)}$	90
U_{∞} (m/s)	0.33
$\rho_s \ (kg/m^3)$	2270
$\rho_p \ (kg/m^3)$	5440
E_s (GPa)	14.5
E_p (GPa)	30.336
h_s (mm)	0.49
$h_p \ (mm)$	0.16
$d_{31} (pC/N)$	-170
$e_{31} (C/m^2)$	-5.157
$\varepsilon_{33}^s \ (nF/m)$	12.653

3.1. Harvested voltage and power

The harvested voltage and harvested electric power are dependent on the electrical load resistance and excitation frequency. Figure 3a shows that the generated voltage over the considered range of excitation frequencies is linearly proportional to the load resistance in the range up to about $R=10^4\Omega$. As the resistance value is increased further, the voltage asymptotically approaches values near 10 V when k=3.78 and between 20 and 30 V at the higher excitation frequencies. These results validate equation (29), which predicts the linear dependence of the harvested voltage on the load resistance at relatively small R values, and non-dependence on the resistance at the higher R values. Figure 3b shows that for each excitation frequency, there is an optimal electrical load resistance at which the harvested electric power is maximum. This optimal value decreases when the reduced frequency is increased from 1.7 to 11.27, in agreement with the analytical prediction presented in equation (30).

In table 2, we compare the harvested power from the current design to values of harvested power from previously published experiments. The experiments include implanting a piezoelectric MFC inside a live fish [22], attaching MFC to a biomimetic prototype inspired by thresher sharks [25], or attaching the MFC to an underwater fish-like bimorph cantilever [23]. A comparison of the results shows that the predictions by the current model are slightly larger but of the same order of magnitude as in the experiments, mostly because of the idealized conditions of the numerical simulations..

Table 2: Comparison with previously published experiments.

Reference	Material	PZT Size (mm^2)	Average power (μW)	Host	Base Excitation
Li et al. [22]	PZT - MFC (3-1)	85×3	9.3 @ 1 Hz and >24 @ 2 Hz	Inside a rainbow trout	Pitching
Cha et al. [25]	PZT - MFC (3-3)	40×7	$0.18 \ @ \ 1.6 \ \mathrm{Hz}$	On biomimetic tail inspired by thresher sharks	Pitching
Erturk and Delporte [23]	PZT - MFC (3-3)	85×28	8000 @ 6.7 Hz	underwater fish-like bimorph cantilever	Heaving
Proposed unimorph tail	PZT - MFC P2 (3-1)	90×90	$23.5 @ 2 Hz and \approx 11000 @ 6.7 Hz$	Attached to biomimetic fish tail (unimorph)	Pitching

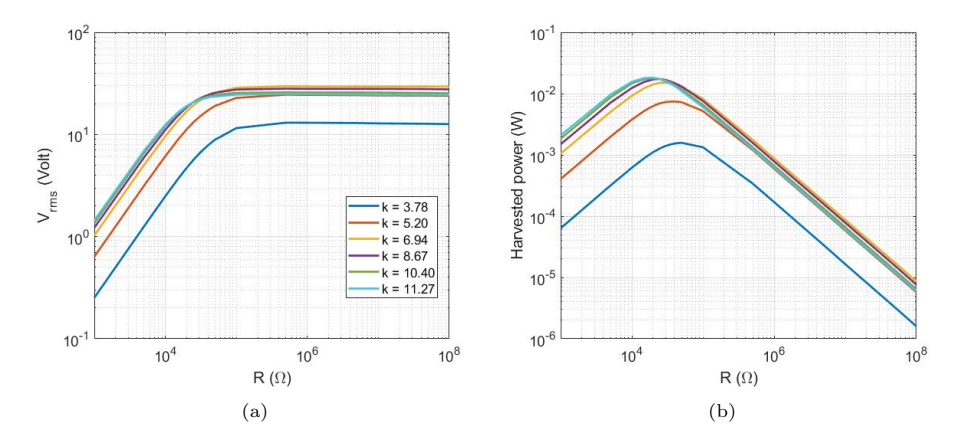


Figure 3: (a) Generated voltage, and (b) harvested electric power variation with electrical load resistance and reduced frequency.

3.2. Impact of energy harvesting on wake vorticity and hydrodynamic forces

The generated hydrodynamic forces are directly related to the vorticity field in the wake of the flapping beam characterized by the shedding of counterrotating vortices that are responsible for thrust generation. Figure 4 compares surface plots of the generated circulation in the wake of the flapping beam with and without attached PZT element for two different excitation frequencies and a load resistance of $R = 2 \times 10^4 \Omega$. At k=2.17, adding a piezoelectric element reduces the circulation over a broad region of the wake, indicating a reduction in the propulsive force. In contrast, at k=3.8, adding the piezoelectric element increases the circulation and as such the propulsive force. The impact of adding a piezoelectric element on the circulation in the wake over the whole range of reduced frequencies is assessed in figure 5, which compares the maximum generated circulation amplitude by the flapping and unimorph beams. The plots show that at excitation frequencies with k < 2.17, the generated circulation levels are slightly reduced when the PZT element was attached. The highest reduction is about 10%, from 15.7×10^3 to 14.2×10^3 , at k = 2.17. For k > 4, the piezoelectric element results in significantly increased circulation in the wake, with a maximum increase by about four folds near k=6.

Time histories of the transverse force, thrust, and hydrodynamic power coefficients for the bare and unimorph beams at the reduced frequency k=4 are compared in figure 6. The resistance value in the unimorph beam was set to $2 \times 10^4 \Omega$. Figure 6a shows that the amplitude of the transverse force coefficient increases by about 60% when the PZT element is attached. In both cases, however, the mean value is zero due to the symmetry of the imposed tail flapping motion. The mean values of the thrust and hydrodynamic power coefficients increase when the PZT layer is attached, as shown in figures 6b and c, which demonstrates that while the PZT layer can increase the thrust, a higher level of hydrodynamic power is required to generate the increased thrust.

To assess more broadly the impact of the PZT element on the hydrodynamic performance, we compare in figure 7 the thrust and hydrodynamic power coefficients, and the efficiency as defined in equation (34) of the bare and unimorph beams over the whole range of excitation frequencies. Figure 7a shows no thrust

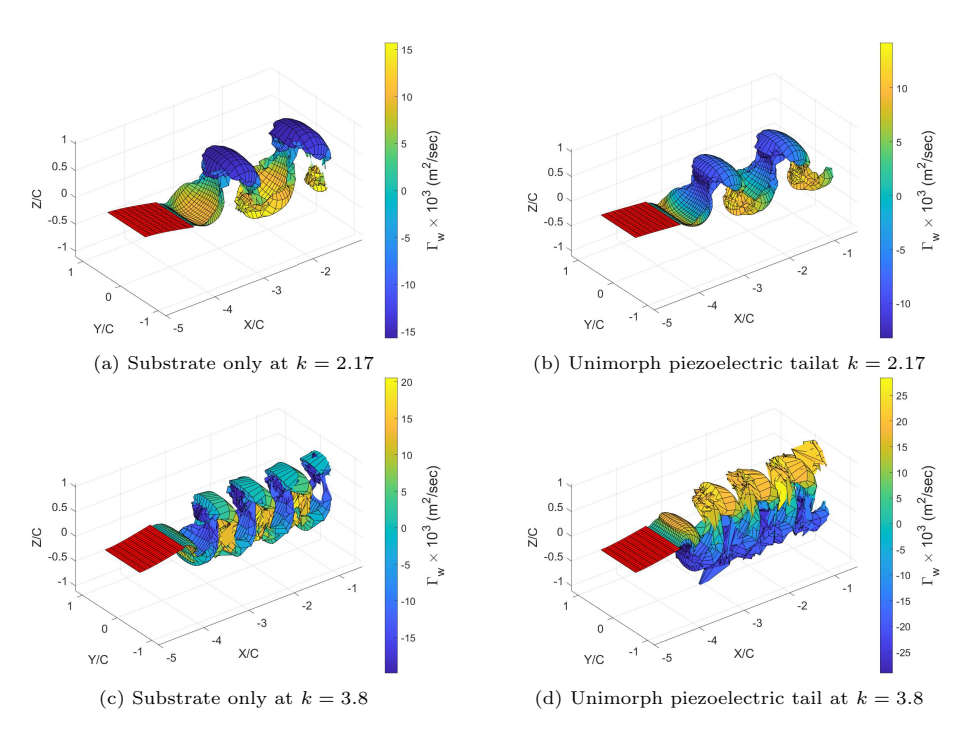


Figure 4: Comparison of surface plots of the circulation in the wake of the tail with and without the PZT element under two different excitation frequencies at k=2.17 and 3.8.

generation at very low forcing frequencies (k < 1.7). In the range 1.7 < k < 3.3, attaching the PZT layer decreases slightly the thrust coefficient. In contrast, over the range of higher excitation frequencies k > 4, adding the piezoelectric element appreciably increases the thrust coefficient. The maximum increase of about seven folds takes place at k=6. The variations in the power coefficient follow closely the variations of the thrust coefficient as shown in figure 7b. In the range of k < 3.3, the required power is about the same. In the higher frequency range of k > 4, the required power is larger. The maximum increase is at k = 6, the same reduced frequency where maximum thrust is obtained. To get a better perspective on the impact of adding the piezoelectric element on the hydrodynamic performance, we present in Figure 7c the variations in the propulsive efficiency with and without the piezoelectric element over the range of excitation frequencies. The plots show that attaching the piezoelectric element decreases the propulsive efficiency over the whole range of excitation frequencies. In the range of k < 3.3, the efficiency decreases from about 35% to slightly less than 30%. In the range of k > 4, the decrease is more significant from about 35% to 20% when attaching the PZT layer. Recognizing that fish skin, tendons, and bones can act like springs to change the stiffness and adapt to different swimming conditions, it is plausible that the fish can realize a better performance when a PZT layer is attached by its ability to change its stiffness.

3.3. Validation and significance of analytical predictions

Validation of the analytical expression for the power, as derived above, is demonstrated in the plots of figure 8, which show agreement between the analytical predictions and numerical simulations for two different excitation fre-

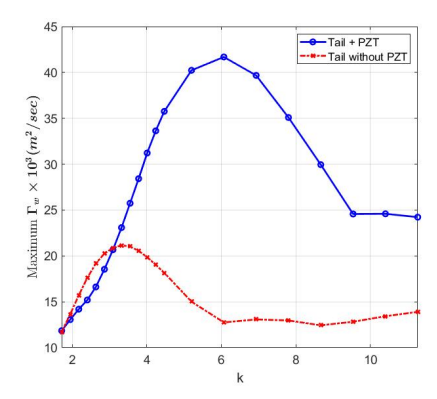


Figure 5: Variations of the maximum circulation in the wake of the tail with and without the PZT element with the excitation reduced frequency k at constant excitation amplitude.

quencies over the range of considered electrical loads. This agreement validates the dependence of the harvested power on the square of the slope of the trailing edge as predicted by the power equation in section 2.1.2. To assess the impact of the load resistance and excitation frequency on the slope of the trailing edge, we plot in figure 9 the simulated time variations of the slope of the trailing edge for two different frequencies, k = 5.2 and 11.27, and two different electric loads, 10^3 and $10^8\Omega$, for each frequency. The plots show that the amplitude of the slope is about the same in all cases. Consequently, beyond specific values of load resistance and excitation frequencies, the generated voltage can only be slightly impacted, as also shown in figure 3a.

The dependence of the performance of unimorph beam in terms of generating thrust and electric energy on the displacement amplitude and slope of the trailing edge is illustrated in figure 10. The displacement amplitude, A, is normalized by that of the corresponding rigid tail, A_{∞} , under the same excitation amplitude, 8°, over the range of excitation frequencies. The plots show that the PZT element changes the amplitude of the response. In the relatively low regime of excitation frequencies, k < 3 the PZT causes a decrease in the amplitude of the response. In the higher excitation frequency regime k > 4, the response is significantly higher. It is also noted that the maximum response shifts from taking place near k=2.6 for the bare beam to taking place near k=5.2 for the unimorph beam, indicating a shift in the natural coupled frequency. Also, the respective maximum amplitude changes from 1.45 to 1.6. Similar observations can be made about the slope of the trailing edge where the maximum value shifts from taking place at k=4 for the case of the bare beam to near k=7 for the unimorph beam. It is of interest to note that the maximum generated thrust takes place at a reduced frequency between those of the maximum amplitude and maximum slope of the trailing edge, which indicates that the generated thrust depends on both amplitude and slope of the trailing edge. On the other hand, the maximum generated voltage and power happen at exactly the same reduced frequencies where the maximum slope of the trailing edge is observed in the case of the PZT covered beam, indicating the direct dependence of the generated power on the slope of the trailing edge.

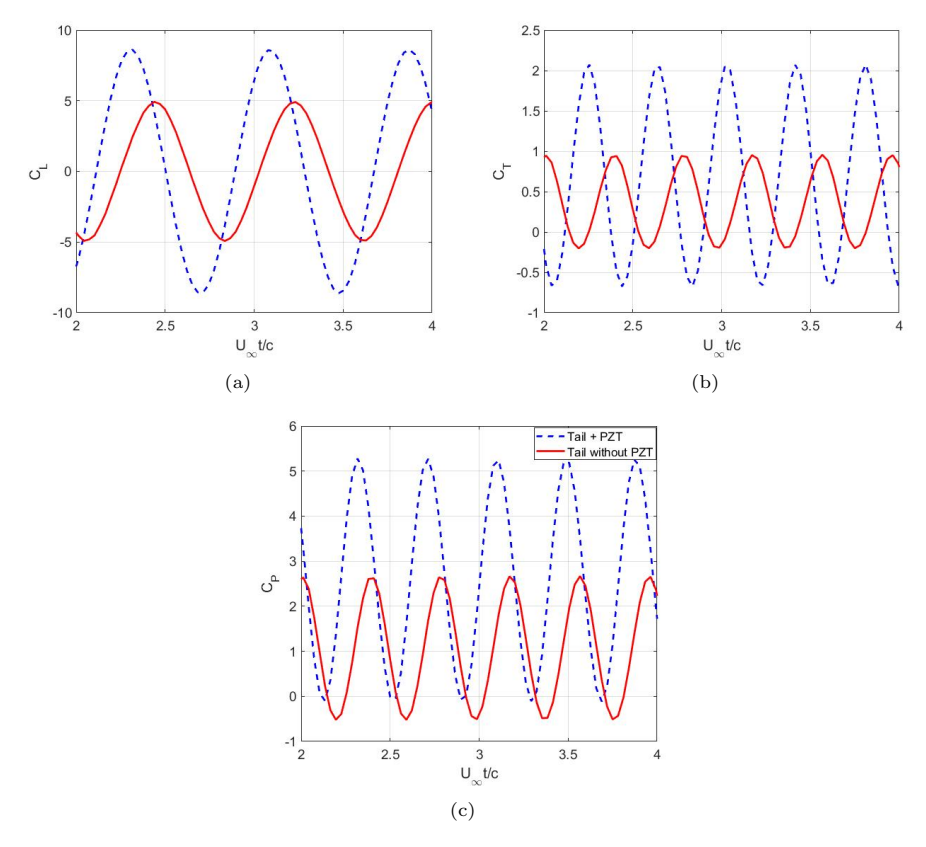


Figure 6: Time histories of (a) transverse force, (b) thrust, and (c) power coefficients at reduced frequency k=4 using non-dimensional time.

${\it 3.4. Balance of hydrodynamic, propulsive and harvested power levels}$

Figures 11a and b show respectively the input and propulsive power variations with excitation frequency and electrical load resistance. The plots show that at reduced frequencies k < 4, the electrical load resistance has no impact on the propulsion performance in terms of the input power required to flap the tail and the generated thrust power. Although the level of harvested power by the PZT element increases exponentially with the increase in the reduced frequency, as shown in figure 11c, its level remains about three orders of magnitude lower than the hydrodynamic or propulsive power. In the range of frequencies 4 < k < 6, the required hydrodynamic power is not impacted while the propulsive power is reduced slightly especially at the optimal load resistance. In this range, the harvested electrical power by the PZT increases by one order of magnitude as shown in figure 11c. In the higher frequency range, k > 6, both required hydrodynamic power and propulsive power are reduced depending on the load resistance. This reduction is not, however, accompanied by a significant increase in the level of harvested power. Clearly, k=6 defines a reduced frequency at which electrical power can be harvested by a PZT element with a minimal impact on the hydrodynamic power or propulsive power significantly.

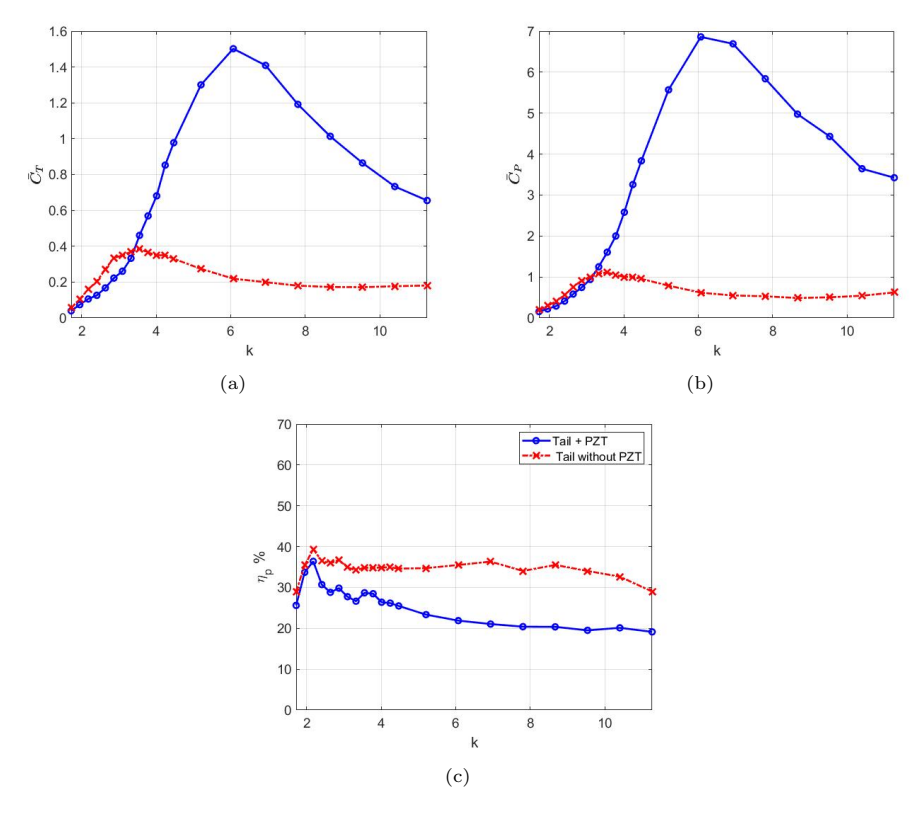


Figure 7: (a) Thrust coefficient, (b) power coefficient, and (c) propulsive efficiency versus reduced frequency.

4. Conclusions

We performed analysis and numerical simulations to assess the level of harvested energy and effects of attaching a PZT element to a deforming part of a fish body such as its tail. The tail with a PZT element was modeled as a deforming unimorph beam subjected to pitching excitation at its root. The analysis provided analytical expressions for the generated voltage and power and their dependence on the slope of the trailing edge. The analysis also shows that the hydrodynamic power and propulsive thrust depend on the amplitude and slope of the trailing edge. In contrast, the harvested electric power depends on the slope of the trailing edge. These results were validated numerically. The numerical simulations showed that attaching a PZT results in a slight reduction of the vorticity field and the thrust force in the low range of excitation frequencies. Conversely, it is more pronounced and results in increased vorticity and larger thrust at higher frequencies. The larger thrust, however, requires a higher level of input hydrodynamic power. The balance of required hydrodynamic power, generated propulsive power and harvested electrical power shows a significant increase initially with the increase in the excitation frequency. However, it is important to identify the frequency at which maximum benefit, in terms of high levels of harvested power without a big impact on the hydrodynamic or propulsive power, is obtained. Because fish skin, tendons, and bones can act like

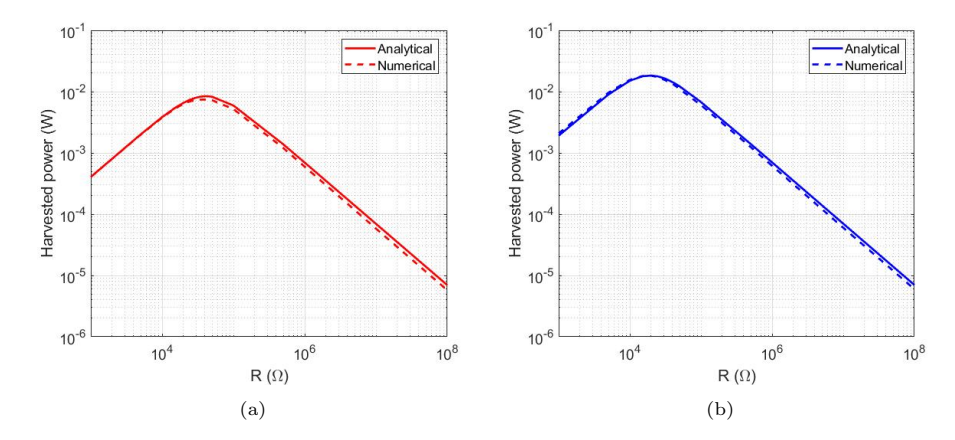


Figure 8: Harvested electric power variation with electrical load resistance for (a) k=5.2, and (b) k=11.27.

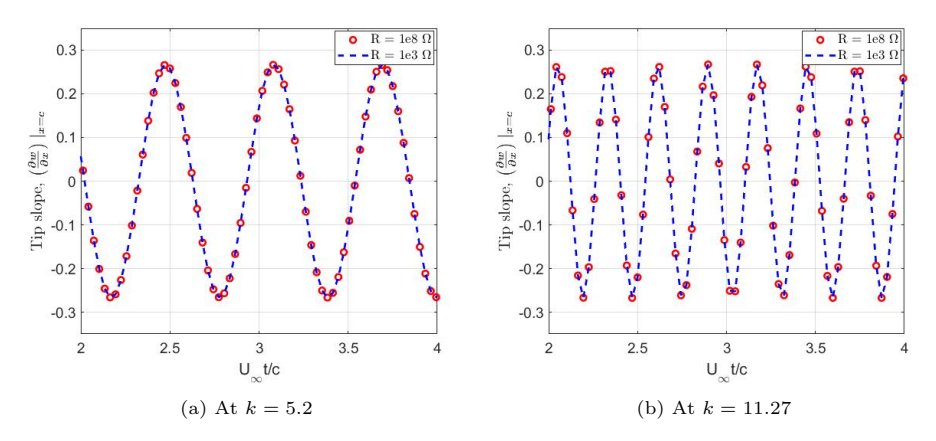


Figure 9: Time history of tail tip slope using the non-dimensional time.

springs to change the stiffness and adapt to different swimming conditions, it is plausible that the fish can realize a better performance when a PZT is attached. The approach and results can be used to identify a reduced frequency at which electrical power can be harvested by a PZT element with a minimal impact on the hydrodynamic power or propulsive power.

5. Acknowledgements

H. Alqaleiby and M. Hajj acknowledge the sponsorship of the NSF under Grant No. 1935954. L. Zuo acknowledges the sponsorship of the NSF under Grant No. 2245117. The authors express their gratitude to Dr. Ahmed Hussein for helping in the modelling and valuable discussion.

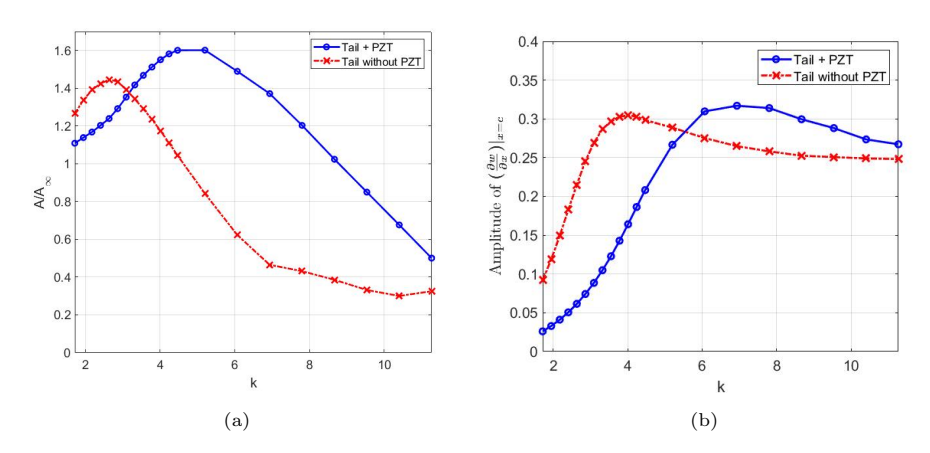


Figure 10: (a) Variations of the peak-to-peak amplitude, and (b) the amplitude of the slope of the trailing edge with the reduced frequency k. A_{∞} is the peak-to-peak amplitude of the rigid tail.

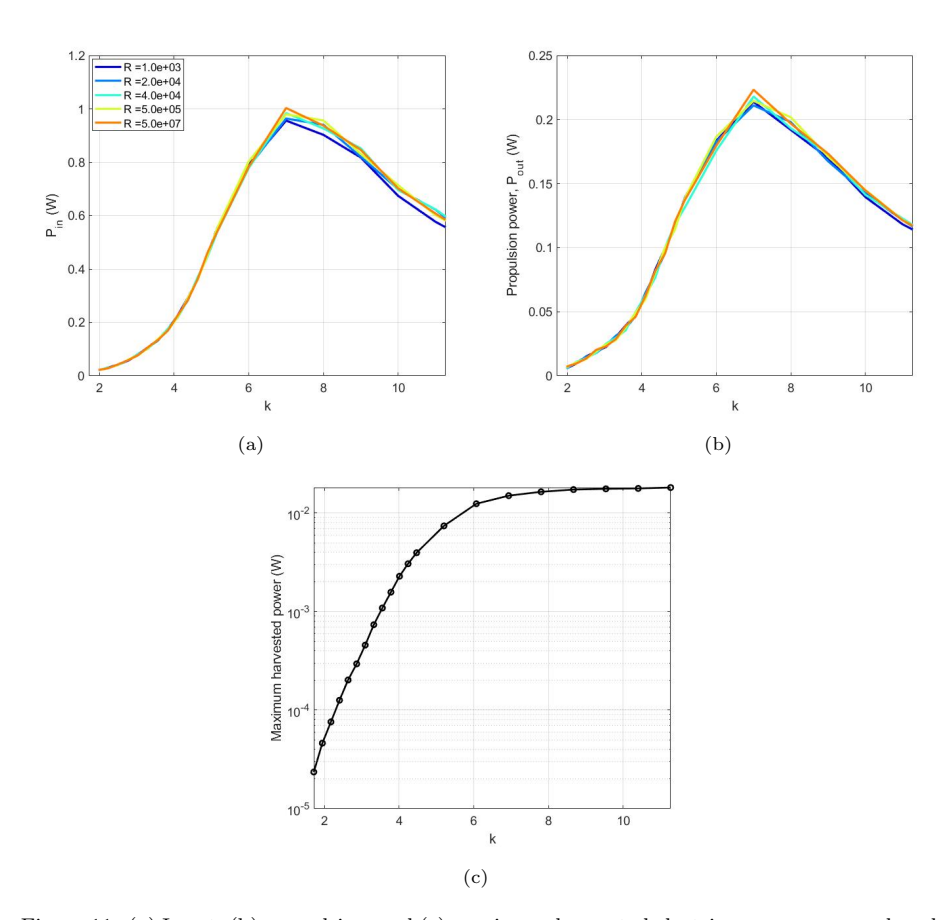


Figure 11: (a) Input, (b) propulsive, and (c) maximum harvested electric power versus reduced frequency for the unimorph PZT tail.

References

- [1] Glenn T Crossin, Michelle R Heupel, Christopher M Holbrook, Nigel E Hussey, Susan K Lowerre-Barbieri, Vivian M Nguyen, Graham D Raby, and Steven J Cooke. Acoustic telemetry and fisheries management. *Ecological Applications*, 27(4):1031–1049, 2017.
- [2] Georgia Macaulay, Fletcher Warren-Myers, Luke T Barrett, Frode Oppedal, Martin Føre, and Tim Dempster. Tag use to monitor fish behaviour in aquaculture: a review of benefits, problems and solutions. *Reviews in Aquaculture*, 13(3):1565–1582, 2021.
- [3] Carl Tamario, Johanna Sunde, Erik Petersson, Petter Tibblin, and Anders Forsman. Ecological and evolutionary consequences of environmental change and management actions for migrating fish. Frontiers in Ecology and Evolution, 7:271, 2019.
- [4] Barbara A Block, Steven LH Teo, Andreas Walli, Andre Boustany, Michael JW Stokesbury, Charles J Farwell, Kevin C Weng, Heidi Dewar, and Thomas D Williams. Electronic tagging and population structure of atlantic bluefin tuna. *Nature*, 434(7037):1121–1127, 2005.
- [5] Heidi Dewar, Steven G Wilson, John R Hyde, Owyn E Snodgrass, Andrew Leising, Chi H Lam, Reka Domokos, James A Wraith, Steven J Bograd, Sean R Van Sommeran, et al. Basking shark (cetorhinus maximus) movements in the eastern north pacific determined using satellite telemetry. Frontiers in Marine Science, 5:163, 2018.
- [6] Camrin D Braun, Gregory B Skomal, Simon R Thorrold, and Michael L Berumen. Movements of the reef manta ray (manta alfredi) in the red sea using satellite and acoustic telemetry. *Marine biology*, 162(12):2351–2362, 2015.
- [7] Ingebrigt Uglem, Tim Dempster, Pål-Arne Bjørn, Pablo Sanchez-Jerez, and Finn Økland. High connectivity of salmon farms revealed by aggregation, residence and repeated movements of wild fish among farms. *Marine Ecology Progress Series*, 384:251–260, 2009.
- [8] Niels Jepsen, Eva B Thorstad, Torgeir Havn, and Martyn C Lucas. The use of external electronic tags on fish: an evaluation of tag retention and tagging effects. *Animal Biotelemetry*, 3(1):1–23, 2015.
- [9] Geoffrey A McMichael, M Brad Eppard, Thomas J Carlson, Jessica A Carter, Blaine D Ebberts, Richard S Brown, Mark Weiland, Gene R Ploskey, Ryan A Harnish, and Z Daniel Deng. The juvenile salmon acoustic telemetry system: a new tool. *Fisheries*, 35(1):9–22, 2010.
- [10] Honghao Chen, Samuel Cartmell, Qiang Wang, Terence Lozano, Z Daniel Deng, Huidong Li, Xilin Chen, Yong Yuan, Mark E Gross, Thomas J Carlson, et al. Micro-battery development for juvenile salmon acoustic telemetry system applications. *Scientific reports*, 4(1):1–5, 2014.

- [11] Guangwei Shi, Ting Tan, Shen Hu, and Zhimiao Yan. Hydrodynamic piezoelectric energy harvesting with topological strong vortex by forced separation. *International Journal of Mechanical Sciences*, 223:107261, 2022.
- [12] Weipeng Sun, Daoli Zhao, Ting Tan, Zhimiao Yan, Pengcheng Guo, and Xingqi Luo. Low velocity water flow energy harvesting using vortex induced vibration and galloping. *Applied Energy*, 251:113392, 2019.
- [13] Rakesha Chandra Dash, Dipak Kumar Maiti, and Bhrigu Nath Singh. Dynamic stability and performance analysis of a galloping-based piezoelectric energy harvester for different order representations of the aerodynamic force. *International Journal of Non-Linear Mechanics*, 121:103463, 2020.
- [14] Chenxia Wan, Haigang Tian, Xiaobiao Shan, and Tao Xie. Enhanced performance of airfoil-based piezoelectric energy harvester under coupled flutter and vortex-induced vibration. *International Journal of Mechanical* Sciences, 241:107979, 2023.
- [15] Ahmed A Hamada and Mirjam Fürth. Ground effect on current energy harvesting from a freely-oscillating circular cylinder at low reynolds number. In *International Conference on Offshore Mechanics and Arctic Engineering*, volume 85192, page V009T09A003. American Society of Mechanical Engineers, 2021.
- [16] Hai-Tao Li, He Ren, Fan Cao, and Wei-Yang Qin. Improving the galloping energy harvesting performance with magnetic coupling. *International Journal of Mechanical Sciences*, 237:107785, 2023.
- [17] Zhiyuan Li, Shengxi Zhou, and Xia Li. A piezoelectric–electromagnetic hybrid flutter-based wind energy harvester: Modeling and nonlinear analysis. *International Journal of Non-Linear Mechanics*, 144:104051, 2022.
- [18] David Gibus, Pierre Gasnier, Adrien Morel, Fabien Formosa, Ludovic Charleux, Sébastien Boisseau, Gaël Pillonnet, Carlos Augusto Berlitz, Anthony Quelen, and Adrien Badel. Strongly coupled piezoelectric cantilevers for broadband vibration energy harvesting. Applied Energy, 277:115518, 2020.
- [19] A Mujtaba, U Latif, E Uddin, MY Younis, M Sajid, Z Ali, and A Abdelkefi. Hydrodynamic energy harvesting analysis of two piezoelectric tandem flags under influence of upstream body's wakes. Applied Energy, 282:116173, 2021.
- [20] Zhemin Wang, Yu Du, Tianrun Li, Zhimiao Yan, and Ting Tan. A flute-inspired broadband piezoelectric vibration energy harvesting device with mechanical intelligent design. Applied Energy, 303:117577, 2021.
- [21] Haigang Tian, Xiaobiao Shan, Xia Li, and Junlei Wang. Enhanced airfoil-based flutter piezoelectric energy harvester via coupling magnetic force. *Applied Energy*, 340:120979, 2023.
- [22] Huidong Li, Chuan Tian, Jun Lu, Mitchell J Myjak, Jayson J Martinez, Richard S Brown, and Zhiqun Daniel Deng. An energy harvesting underwater acoustic transmitter for aquatic animals. *Scientific reports*, 6(1):1–9, 2016.

- [23] Alper Erturk and Ghislain Delporte. Underwater thrust and power generation using flexible piezoelectric composites: an experimental investigation toward self-powered swimmer-sensor platforms. Smart materials and Structures, 20(12):125013, 2011.
- [24] Michael W Shafer, Robert MacCurdy, and Ephrahim Garcia. Testing of vibrational energy harvesting on flying birds. In Smart Materials, Adaptive Structures and Intelligent Systems, volume 56048, page V002T07A004. American Society of Mechanical Engineers, 2013.
- [25] Youngsu Cha, Woojin Chae, Hubert Kim, Horace Walcott, Sean D Peterson, and Maurizio Porfiri. Energy harvesting from a piezoelectric biomimetic fish tail. Renewable Energy, 86:449–458, 2016.
- [26] Youngsu Cha, Matteo Verotti, Horace Walcott, Sean D Peterson, and Maurizio Porfiri. Energy harvesting from the tail beating of a carangiform swimmer using ionic polymer–metal composites. *Bioinspiration & biomimetics*, 8(3):036003, 2013.
- [27] Chuguo Zhang, Zhihao Zhao, Ou Yang, Wei Yuan, Linglin Zhou, Xing Yin, Li Liu, Yanhong Li, Zhong Lin Wang, and Jie Wang. Bionic-fin-structured triboelectric nanogenerators for undersea energy harvesting. Advanced Materials Technologies, 5(9):2000531, 2020.
- [28] Feng Qian, Mingyi Liu, Jianuo Huang, Jiajun Zhang, Hyunjun Jung, Zhiqun Daniel Deng, Muhammad R Hajj, and Lei Zuo. Bio-inspired bistable piezoelectric energy harvester for powering animal telemetry tags: Conceptual design and preliminary experimental validation. Renewable Energy, 187:34–43, 2022.
- [29] R Salazar, G Taylor, MSU Khalid, and A Abdelkefi. Optimal design and energy harvesting performance of carangiform fish-like robotic system. Smart Materials and Structures, 27(7):075045, 2018.
- [30] R Salazar and A Abdelkefi. Nonlinear analysis of a piezoelectric energy harvester in body undulatory caudal fin aquatic unmanned vehicles. Applied Energy, 263:114627, 2020.
- [31] Xiaojing Sun, Jihua Zhang, and Diangui Huang. Energy harvesting characteristics of an inward-type flow device undulating in a fish-like motion. European Journal of Mechanics-B/Fluids, 79:419–427, 2020.
- [32] Weixing Chen, Yibo Hu, Yinghan Peng, Chong Zhu, Weidong Zhang, and Feng Gao. Energy harvesting by flexible piezoelectric generator for tag attached on the oscillating fish tail. *Available at SSRN 4103969*, 2022.
- [33] Shun-Qi Zhang, Ya-Xi Li, and Rüdiger Schmidt. Modeling and simulation of macro-fiber composite layered smart structures. *Composite Structures*, 126:89–100, 2015.
- [34] J Katz and D Weihs. Hydrodynamic propulsion by large amplitude oscillation of an airfoil with chordwise flexibility. *Journal of Fluid Mechanics*, 88(3):485–497, 1978.

- [35] Peter A. Dewey, Birgitt M. Boschitsch, Keith W. Moored, Howard A. Stone, and Alexander J. Smits. Scaling laws for the thrust production of flexible pitching panels. *Journal of Fluid Mechanics*, 732:29–46, 2013.
- [36] Ahmed A Hussein, Saad A Ragab, Muhammad R Hajj, and Mayuresh J Patil. Material and geometric effects on propulsion of a fish tail. *Bioinspiration & Bioinmetics*, 16(6):066008, 2021.
- [37] Alper Erturk and Daniel J Inman. A distributed parameter electromechanical model for cantilevered piezoelectric energy harvesters. *Journal of vibration and acoustics*, 130(4), 2008.
- [38] ANSI/IEEE Std 176-1987. IEEE Standard on Piezoelectricity, 1988.
- [39] Laurent. Schwartz. Théorie des Distributions. Hermann, Paris, France, 1978.
- [40] Alper Erturk and Daniel J Inman. An experimentally validated bimorph cantilever model for piezoelectric energy harvesting from base excitations. Smart materials and structures, 18(2):025009, 2009.
- [41] T Tan, Z Yan, and M Hajj. Electromechanical decoupled model for cantilever-beam piezoelectric energy harvesters. Applied Physics Letters, 109(10):101908, 2016.
- [42] EH Atta, OA Kandil, DT Mook, and AH Nayfeh. Unsteady aerodynamic loads on arbitrary wings including wing-tip and leading-edge separation. AIAA paper, 156:1977, 1977.
- [43] Joseph Katz and Allen Plotkin. *Low-speed aerodynamics*, volume 13. Cambridge university press, 2001.
- [44] Mehdi Ghommem, Muhammad R Hajj, Dean T Mook, Bret K Stanford, Philip S Beran, Richard D Snyder, and Layne T Watson. Global optimization of actively morphing flapping wings. *Journal of Fluids and Structures*, 33:210–228, 2012.
- [45] M Ghommem, A Abdelkefi, AO Nuhait, and MR Hajj. Aeroelastic analysis and nonlinear dynamics of an elastically mounted wing. *Journal of Sound* and Vibration, 331(26):5774–5787, 2012.
- [46] Abdessattar Abdelkefi, Mehdi Ghommem, Abdullah O Nuhait, and MR Hajj. Nonlinear analysis and enhancement of wing-based piezoaeroelastic energy harvesters. *Journal of Sound and Vibration*, 333(1):166–177, 2014.
- [47] Nathan M Newmark. A method of computation for structural dynamics. Journal of the engineering mechanics division, 85(3):67–94, 1959.
- [48] Saad A Ragab and Hassan E Fayed. *Introduction to Finite Element Analysis for Engineers*. Boca Raton, FL: CRC Press, 2017.
- [49] James L Tangorra, George V Lauder, Ian W Hunter, Rajat Mittal, Peter GA Madden, and Meliha Bozkurttas. The effect of fin ray flexural rigidity on the propulsive forces generated by a biorobotic fish pectoral fin. Journal of Experimental Biology, 213(23):4043–4054, 2010.

- [50] Intesaaf Ashraf, Hanaé Bradshaw, Thanh-Tung Ha, José Halloy, Ramiro Godoy-Diana, and Benjamin Thiria. Simple phalanx pattern leads to energy saving in cohesive fish schooling. *Proceedings of the National Academy* of Sciences, 114(36):9599–9604, 2017.
- [51] Yuanhao Zhang, Rongjie Kang, Donato Romano, Paolo Dario, and Zhibin Song. Experimental research on the coupling relationship between fishtail stiffness and undulatory frequency. *Machines*, 10(3):182, 2022.